Supplementary information for "Magnetically-controlled vortex dynamics in a ferromagnetic superconductor"

Joseph Alec Wilcox,[1,*] Lukas Schneider,[2] Estefani Marchiori,[2] Vadim Plastovets,[3] Alexandre Buzdin,[3] Pardis Sahafi,[4,5] Andrew Jordan,[4,5] Raffi Budakian,[4,5] Tong Ren,[6] Ivan Veshchunov,[6] Tsuyoshi Tamegai,[6] Sven Friedemann,[7] Martino Poggio,[2] and Simon John Bending[1]

[1]*Department of Physics, University of Bath, Claverton Down, Bath, BA2 7AY, United Kingdom*
[2]*Department of Physics, University of Basel, Klingelbergstrasse 82, 4056 Basel, Switzerland*
[3]*University of Bordeaux, LOMA UMR-CNRS 5798, F-33405 Talence Cedex, France*
[4]*Department of Physics and Astronomy, University of Waterloo, Waterloo, Canada*
[5]*Institute for Quantum Computing, University of Waterloo, Waterloo, Canada*
[6]*Department of Applied Physics, The University of Tokyo, 7-3-1 Hongo, Bunkyo-ku, Tokyo 113-8565, Japan*
[7]*H. H. Wills Physics Laboratory, University of Bristol, Bristol, BS8 1TL, United Kingdom*

SUPPLEMENTARY NOTE 1: FERROMAGNETIC TRANSITION

In the main text (Fig. 1), magnetic characterisation data for $EuFe_2(As_{1-x}P_x)_2$ samples S1 and S2 are presented. In the zero-field cooled curve of S1 the superconducting transition is clearly visible, while the ferromagnetic transition exhibits an unusual form. Figure 1 shows a field cooled measurement of S1 in a larger field, exhibiting a more typical form. The crossover from paramagnetic to ferromagnetic behaviour is evident at $T \approx 19.3$ K, while the superconducting transition at $T \approx 24.5$ K is now no longer visible.

SUPPLEMENTARY NOTE 2: COMPARISON OF REVERSIBLE MAGNETISATION IN SAMPLES S1 AND S2

In the main text we discuss the differences in the magnetic characterisation evident in the magnetic hysteresis loops of the two samples S1 ($T_{\mathrm{FM}} \approx 19.3$ K $< T_c \approx 24.5$ K) and S2 ($T_c \approx 12.5$ K $< T_{\mathrm{FM}} \approx 19.3$ K). The two samples exhibit similar temperature dependencies of their susceptibilities, but markedly different coercive fields. We argue that the measured magnetic irreversibility is not caused by ferromagnetic domain pinning but by irreversible vortex dynamics that is a result of the presence of both the superconducting and ferromagnetic orders.

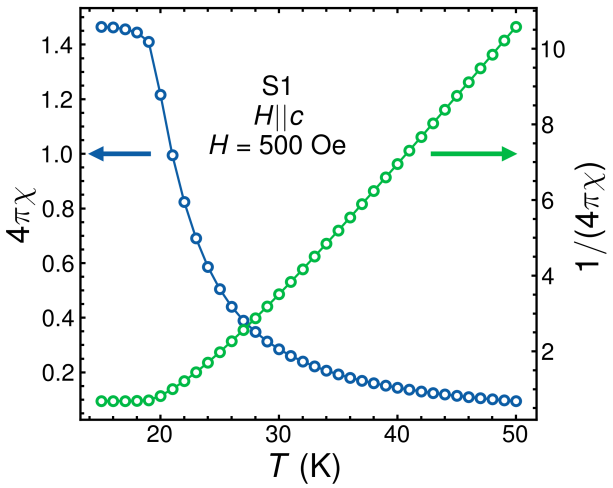

Supplementary Figure 1. Ferromagnetic transition in sample S1. Field-cooled measurement of the magnetic susceptibility $\chi = M/H$ for $EuFe_2(As_{1-x}P_x)_2$ sample S1 in an applied field of 500 Oe oriented parallel to the crystalline c-axis.

* Corresponding author: jaw73@bath.ac.uk

The reversible component of the magnetisation is $M_{\rm rev}(H) = (M_{\rm upp}(H) - M_{\rm low}(H))/2$, where $M_{\rm upp}(H)$ and $M_{\rm low}(H)$ are the total magnetisation measured in the upper and lower branches of the hysteresis loop. Figure 2 shows a comparison of $M_{\rm rev}$ between samples S1 and S2 at a different temperatures with the two samples in various magnetic phases: paramagnetic (PM), superconducting (SC), ferromagnetic (FM), and simultaneously superconducting and ferromagnetic (SC+FM). The response of either sample can be scaled onto the other with a single field-independent, weakly temperature-dependent scale factor. The scale factor arises in part due to the different sample volumes and also their different aspect ratios, and these two contributions will affect the ferromagnetic and superconducting portion of the sample response differently.

Given that the two samples exhibit the same reversible magnetic response across the whole temperature range examined, we conclude that there is no significant difference in the paramagnetic and ferromagnetic states of the two samples. Furthermore, in the region where S1 is both SC and FM, and S2 is only FM (i.e. Supplementary Figure 2, $T = 16$ K), S2 exhibits a very soft form of ferromagnetism with $H_c \sim 0$ until $T < T_c$ while, contrastingly, H_c in S1 grows quickly as T is reduced (Fig. 1f). Since we have argued that the reversible magnetic states of the two samples are very similar, this difference in irreversibility is then precisely due to a combination of the superconducting and ferromagnetic states and not related to the intrinsic, highly-reversible ferromagnetic state that the two samples share.

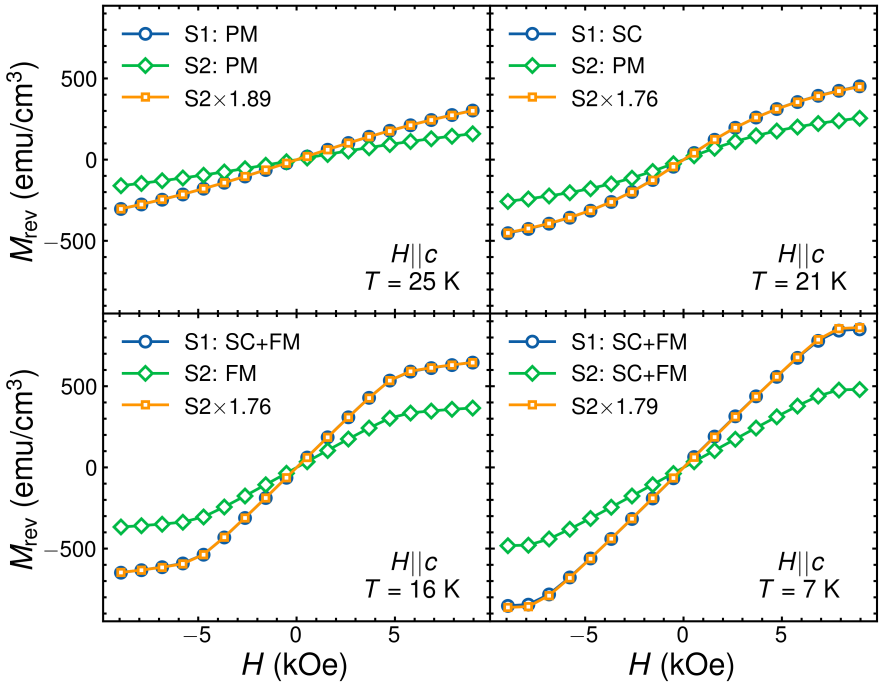

Supplementary Figure 2. Comparison of the reversible component of the magnetisation $M_{\rm rev}(H)$ between samples S1 and S2 at various temperatures. The responses of the two samples scale very well with an H-independent, weakly T-dependent scale factor.

SUPPLEMENTARY NOTE 3: ESTABLISHING THE CRITICAL STATE

In order to make a valid analysis based on the critical state model it is necessary to ensure that the sample has reached full magnetic flux penetration[1–3]. Supplementary Figure 3a shows magnetic hysteresis curves measured in sample S1 at $T = 5$ K with increasing maximum fields $\pm H_{\rm max}$. The initial measurement, $H_{\rm max} = 1$ kOe, was made after zero-field cooling the sample from above T_c to 5 K. The field was increased from zero to $+H_{\rm max}$, then reversed to $-H_{\rm max}$, and finally increased back to $H_{\rm max}$ once more. The subsequent loops were made by continuing the cycle of $+H_{\rm max}$ to $-H_{\rm max}$ and back again, using the new, larger value of $H_{\rm max}$. Additionally, no further repeats of the zero-field cooled process were made. In doing so, we can see how the irreversible state evolves with $H_{\rm max}$ and at what point full flux penetration is achieved.

In Supplementary Figure 3a, the initial diamagnetic response of the sample can be seen in the first loop, though this fairly quickly gives over to the ferromagnetic response as H_p, the field of first flux penetration, is exceeded. After the completion of the first curve, all the subsequent curves to increasingly larger values of $H_{\rm max}$ can be seen to trace out approximately the same upper and lower branches that are centred on a shared reversible magnetisation $M_{\rm rev}$. As noted in the main text, the form of the magnetic irreversibility is superconducting in nature which is evident due to the jump in M at the point of field-sweep

reversal at $\pm H_{\rm max}$[4]. This contrasts to ferromagnetic irreversibility where the magnitude of M does not increase under the same circumstances, only remaining or decreasing smoothly from its maximum achieved at $\pm H_{\rm max}$[5].

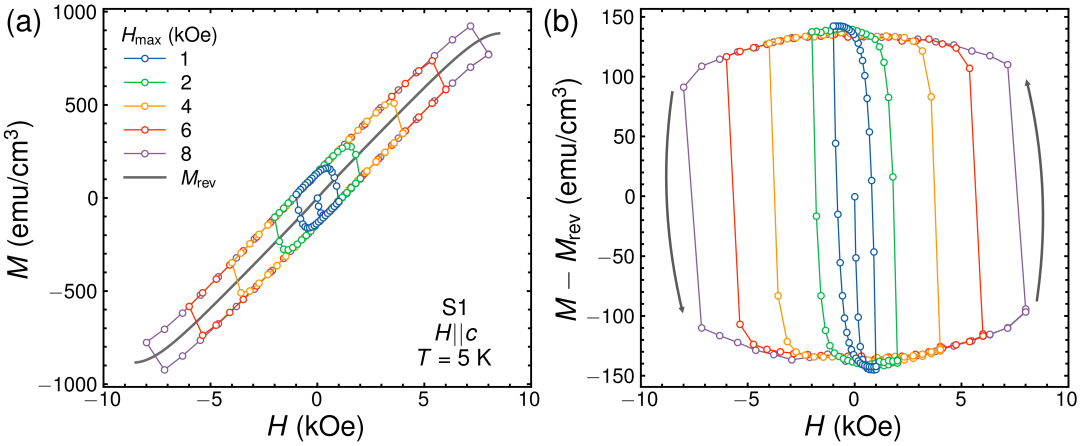

Supplementary Figure 3. **Magnetic hysteresis loops with increasing maximum field.** (a) Total magnetisation M of sample S1 measured at $T = 5$ K. (b) The irreversible portion of the total magnetisation from the curves in (a). The grey arrows indicate the direction of the change in $M_{\rm irr}$ once $H_{\rm max}$ is reached and subsequently $|H|$ is reduced.

Supplementary Figure 3b shows the isolated, irreversible portion of the magnetisation $M_{\rm irr} = M - M_{\rm rev}$ from the hysteresis loops in Supplementary Figure 3a. On closer inspection, while there is good overlap of the loops starting from the initial measurement with $H_{\rm max} = 1$ kOe, there is a slight discrepancy around $H = 0$. It is not until the curve with $H_{\rm max} = 4$ kOe that near-perfect overlap with all subsequent curves (i.e. 6 and 8 kOe) is established, indicating that the critical state is fully realised within the sample. Therefore, the field excursions of ± 10 kOe in the magnetic hysteresis loops presented in Fig. 1e are more than sufficient to establish the critical state, leading to the analysis and presentation of $J_c(T)$ in Fig. 2c. Finally, in Supplementary Figure 3b, we also see the clear jumps in magnetisation at the extremes of the loops, as emphasised by the grey arrows. This reversal of the critical state requires a finite window $\Delta H \lesssim 1$ kOe to fully complete, and therefore the calculation of $J_c \propto \Delta M$ should also be avoided in this region (see main text Methods).

SUPPLEMENTARY NOTE 4: EXAMPLE MAGNETIC RELAXATION MEASUREMENTS

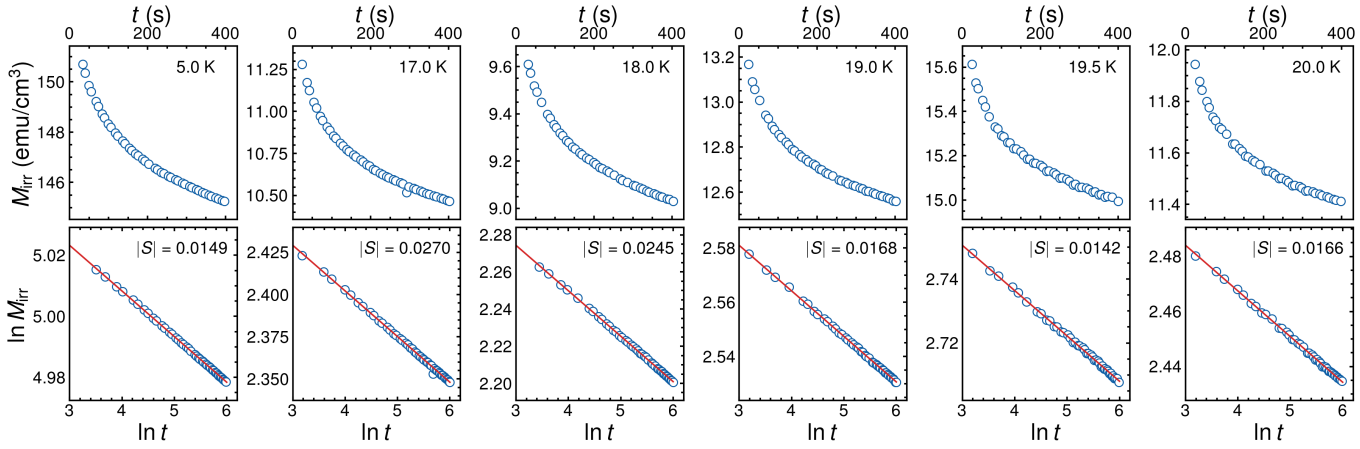

Supplementary Figure 4. **Example relaxation measurement data.** Relaxation measurement data for sample S1 measured in a final field $H_f = -76$ Oe, taken at a selection of temperatures. Left column: the irreversible component of the total magnetisation, $M_{\rm irr}(t)$, shows a characteristic logarithmic decay. Right column: the normalised relaxation rate, S, is determined as the slope of a linear fit to $\ln M_{\rm irr}$ vs. $\ln t$.

Supplementary Figure 4 shows example magnetic relaxation data taken in a final measurement field of $H_f = -76$ Oe. The selection of temperatures includes the very lowest temperature measured as well as the range of temperature for which

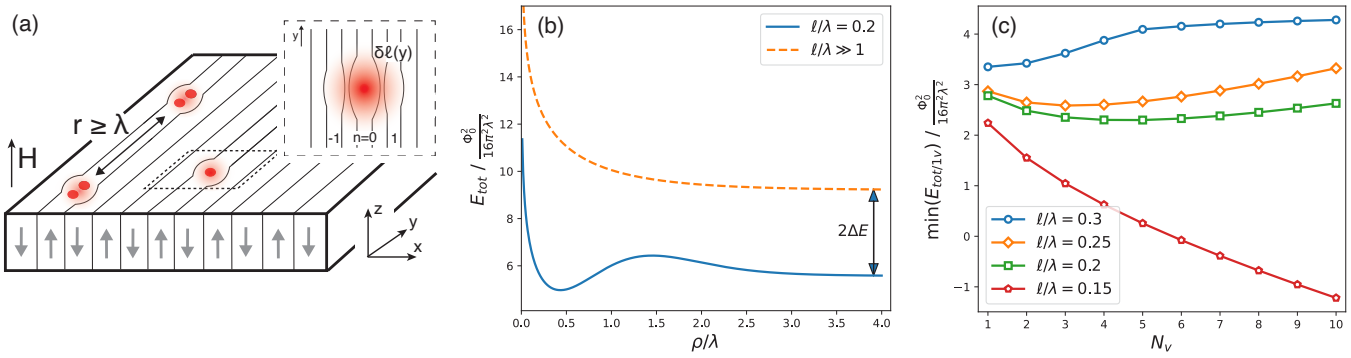

Supplementary Figure 5. **Vortex polaron model and calculations.** (a) Sketch of the vortex polaron formation and example of the vortex polaron clustering. (b) Energy of two interacting vortices $E_{tot}(\rho)$ [Eq. (S.10)] with ($\ell/\lambda = 0.2$) and without ($\ell/\lambda \gg 1$) polaron effect. (c) Bound energy per one vortex minE_{tot} [Eq. (S.12)] in the isolated cluster of N_v vortices. For both plots $\xi/\lambda = 0.01$.

anomalous $S(T)$ behaviour was observed (Fig. 2, attributed to vortex polaron dynamics). The time dependence of the irreversible magnetisation, $M_{\rm irr}(t)$, displays a very clear, characteristic logarithmic decay for all temperatures. The normalised relaxation rate, S, is determined as the slope of a linear fit to $\ln M_{\rm irr}$ vs $\ln t$[6].

SUPPLEMENTARY NOTE 5: THEORETICAL MODEL FOR VORTEX POLARONS IN FERROMAGNETIC SUPERCONDUCTORS

Here we present a theoretical model of the vortex polaron (VP) formation in the domains of a ferromagnetic superconductor. We give a qualitative explanation of the physical origin of the VP, followed by the corresponding calculations.

A. Summary

The system we study is a superconducting ferromagnet with a domain wall (DW) structure of period ℓ. Suppose that an applied external magnetic field induces a single Abrikosov vortex with a size of the order of the London penetration depth λ in a domain of the same orientation (see Supplementary Figure 5a). If the domain width is smaller than λ, which is the case at $T \lesssim T_{\rm SC}$ (Fig. 3c), then the vortex magnetic field will locally expand the hosting magnetic domain. This perturbation, in turn, reduces the electromagnetic energy of the entire system with the only controlling parameter ℓ/λ. In fact, this is a prerequisite for the emergence of a vortex-generated magnetic polaron effect. The VPs can move along the domain and notably interact with each other. As we will show, the magnetic domain is able to mediate the long-range attraction between the vortices, giving rise to the molecule-like few-VPs clusters ($N_v \sim 2-3$) with the inner size $\ell \lesssim \rho_0 \lesssim \lambda$. With the decrease of the domain size ℓ the attraction strength grows and multi-VP clusters ($N_v \gg 1$) can appear, resembling the vortex "bubbles" in the experimental images (see Figs. 4d and e) due to their small inner size.

B. Physical model

Consider a ferromagnet film with the equilibrium domain structure $\mathbf{M}_0(x) = \pm\bar{M}_0\mathbf{z}_0$ ($\bar{M}_0 = $ const) with the period ℓ. The thickness of the film is assumed to be large enough ($d_{\rm F} > \lambda$) so that one can neglect any stray fields and treat the system as homogeneous in the z-direction. Thus, the corresponding magnetic field generated by the domains reads as[7]

$$\mathbf{B}_0(x) = \frac{16\pi\bar{M}_0}{\ell}\sum_k \frac{q}{q^2+\lambda^{-2}}\sin(q(x+\ell/2))\mathbf{z}_0, \tag{S.1}$$

where $q = (2k+1)\pi/\ell$ and k is integer. The Abrikosov vortex is situated at the origin and has a magnetic field distribution $\mathbf{B}_v(\mathbf{r}) = (\Phi_0/2\pi\lambda^2)K_0(|\mathbf{r}|/\lambda)$, where $\Phi_0 = hc/2e$ is the magnetic flux quantum[8]. Within the framework of the London

approximation the total electromagnetic energy of the system per unit length L_z is

$$F = \frac{1}{8\pi}\int d^2r\Big(\mathbf{B}-4\pi\mathbf{M}\Big)^2 + \lambda^2\Big(\nabla\times(\mathbf{B}-4\pi\mathbf{M})\Big)^2. \tag{S.2}$$

The appearance of the polaron effect can be obtained within the perturbation approach. Let us introduce a local distortion of the domain created by the vortex as $\mathbf{M}_0(\mathbf{r})+\mathbf{M}_1(\mathbf{r})$, assuming $\mathrm{div}\mathbf{M}_1(\mathbf{r})=0$. The perturbation of the magnetic field $\mathbf{B}_1(\mathbf{r})$ should be found independently using the linear London equation $\nabla^2\big(\mathbf{B}_1-4\pi\mathbf{M}_1\big)=\lambda^{-2}\mathbf{B}_1$. Corresponding change in the free energy caused by domain expansion simply reads as

$$\Delta E = \frac{1}{4\pi}\int d^2r\ \mathbf{H}_1(\mathbf{H}_0+\mathbf{B}_v)+\lambda^2(\nabla\times\mathbf{H}_1)(\nabla\times(\mathbf{H}_0+\mathbf{B}_v))+\mathbf{H}_1^2+\lambda^2(\nabla\times\mathbf{H}_1)^2. \tag{S.3}$$

For the illustrative purposes we will use a simple phenomenological model of the vortex-domain interaction, which will provide us with the intuitive results and estimations. We determine the deformation of the domain wall as

$$\begin{aligned} M_1(x,y) =& \bar{M}_0\sum_n \mathrm{sgn}\,(x_n-\ell/2)-\mathrm{sgn}\,(x_n-\ell/2-\delta\ell(y,n)) \\ &+\mathrm{sgn}\,(x_n+\ell/2+\delta\ell(y,n))-\mathrm{sgn}\,(x_n+\ell/2)\,, \end{aligned} \tag{S.4}$$

where $x_n=x-2n\ell$, and $n=0,\pm1,\dots$ is the number of the domain co-directed with the vortex field, starting from the vortex position. The domain profile in the y-direction is approximated by the Gaussian function

$$\delta\ell(y,n)=\delta\ell_0\exp\left(-\frac{y^2}{\lambda^2-(2n\ell)^2}\right)\ f_n. \tag{S.5}$$

The amplitude of the deformation of the n-th domain f_n can be connected to the vortex field as $f_n\approx K_0\big(2|n|\ell/\lambda\big)/K_0(\xi)$ with a standard truncation at ξ. Here $\delta\ell_0$ is a variational parameter of the problem. The naturally emerged parameter ℓ/λ determines both the intensity and the spatial distribution of the DW deformation. In order to find the solution of the London equation with $\mathbf{M}_1$ we utilize the adiabatic approximation taking into account the slow y-dependence of the fields, which is justified by the condition $\delta\ell\ll\lambda$. This gives:

$$\begin{aligned} B_1(x,y) = 4\pi\bar{M}_0\sum_n &\ \mathrm{sgn}\Big(x_n-\ell/2\Big)e^{-\frac{|x_n-\ell/2|}{\lambda}}-\mathrm{sgn}\Big(x_n-\ell/2-\delta\ell(y,n)\Big)e^{-\frac{|x_n-\ell/2-\delta\ell(y,n)|}{\lambda}} \\ &+\mathrm{sgn}\Big(x_n+\ell/2+\delta\ell(y,n)\Big)e^{-\frac{|x_n+\ell/2+\delta\ell(y,n)|}{\lambda}}-\mathrm{sgn}\Big(x_n+\ell/2\Big)e^{-\frac{|x_n+\ell/2|}{\lambda}}, \end{aligned} \tag{S.6}$$

and consequently $H_1(x,y)=B_1(x,y)-4\pi M_1(x,y)$.

C. Vortex polaron energy

The energy decrease associated with the DWs distortion (S.3) can be calculated straightforwardly using Eqs. (S.4-S.6). To facilitate this step we assume $\ell\lesssim\lambda$ and build up a perturbation theory using the length scale ratio ℓ/λ as a small parameter. After some derivation we obtain the function $\Delta E(\delta\ell_0)$, with the minimal (optimal) value

$$\Delta E = -\frac{\Phi_0^2}{32\pi\lambda^2}\frac{C_2^2}{C_1}, \tag{S.7}$$

$$\text{where we have defined}\qquad C_1=\sqrt{\frac{\pi}{2}}\sum_{n=0}^{\lambda/2\ell} f_n^2\sqrt{1-(2n\ell/\lambda)^2}\qquad\text{and}\qquad C_2=\sum_{n=0}^{\lambda/2\ell} f_n e^{-2n\ell/\lambda}.$$

Note that C_2^2/C_1 can be roughly estimated as the number of the domain walls on the scale of the vortex, e.g. $C_2^2/C_1\approx\lambda/2\ell$. Thus, the correction (S.7) renormalizes the single vortex energy $E_v\propto\ln(\lambda/\xi)$ as

$$E_{\mathrm{VP}}=\frac{\Phi_0^2}{16\pi^2\lambda^2}\left[\ln\left(\frac{\lambda}{\xi}\right)-\frac{\pi}{2}\frac{C_2^2}{C_1}\right]. \tag{S.8}$$

which we refer as the vortex polaron energy. As we already mentioned, the strength of the polaron effect is determined in fact only by the ratio ℓ/λ. One may notice that there is a critical regime at roughly $\ell<\pi\lambda/4\ln(\lambda/\xi)$, where the VP energy becomes negative, which means the possibility of VP self-generation. We do not discuss this regime since this was not observed experimentally (see Fig. 4), and instead focus on the VP clustering.

D. Interaction of two vortex polarons

Let us now examine the system of two interacting vortices situated at the distance ρ in the same domain (Supplementary Figure 5a). The mutual perturbation of the domain walls $M_1(x,y) = M_1^{(1)}(x,y) + M_2^{(2)}(x,y+\rho)$ creates an effective force between the vortices, which can be extracted directly from Eq. (S.2) using the phenomenological model (S.4-S.6). The corresponding potential

$$\Delta E_{int}(\rho) = 4\Delta E \frac{1}{C_2} \sum_{n=0}^{\lambda/2\ell} f_n e^{-2n\ell/\lambda} e^{-\frac{\rho^2}{\lambda^2(1-(2n\ell/\lambda)^2)}} - 2\Delta E \frac{\sqrt{\pi/2}}{C_1} \sum_{n=0}^{\lambda/2\ell} f_n^2 \sqrt{1-(2n\ell/\lambda)^2} e^{-\frac{\rho^2}{2\lambda^2(1-(2n\ell/\lambda)^2)}}. \quad \text{(S.9)}$$

alters the standard vortex-vortex repulsion potential E_{v-v}, and the total energy of two VP becomes:

$$\begin{aligned} E_{tot}(\rho) &= 2E_{\text{VP}} + E_{v-v}(\rho) + \Delta E_{int}(\rho) \\ &= \frac{\Phi_0^2}{8\pi^2\lambda^2}\left[\ln\left(\frac{\lambda}{\xi}\right) + K_0\left(\frac{\rho}{\lambda}\right)\right] - 2\frac{\Phi_0^2}{32\pi\lambda^2}\frac{C_2^2}{C_1}\times \\ &\left[1 + 2\frac{1}{C_2}\sum_{n=0}^{\lambda/2\ell} f_n e^{-2n\ell/\lambda} e^{-\frac{\rho^2}{\lambda^2(1-(2n\ell/\lambda)^2)}} - \frac{\sqrt{\pi/2}}{C_1}\sum_{n=0}^{\lambda/2\ell} f_n^2\sqrt{1-(2n\ell/\lambda)^2} e^{-\frac{\rho^2}{2\lambda^2(1-(2n\ell/\lambda)^2)}}\right]. \end{aligned} \quad \text{(S.10)}$$

The profile of the function (S.10) is shown in Supplementary Figure 5b. One can easily estimate the equilibrium distance between the vortices at $\ell \lesssim \lambda$ as

$$\rho_0 \approx \lambda\sqrt{\frac{2}{3\pi}\frac{C_1}{C_2^2}} \approx \sqrt{\frac{4\lambda\ell}{3\pi}}. \quad \text{(S.11)}$$

This means that for $\ell \lesssim \lambda$ the inter-VP distance is $\rho_0 \ll \lambda$, what makes this bound (molecule-like) structure almost indistinguishable from a two-quanta vortex. We note that VPs from different domains can also interact in the x-direction. This question, however, appears to be less relevant and is therefore omitted here.

E. Chain of vortex polarons

Now let us consider a finite chain of vortex polarons N_v, oriented along the y axis with a period ρ. The total energy of this chain per one vortex, accounting for all mutual interactions, can be written as

$$E_{tot/1v}(\rho) = E_v + \Delta E + \sum_{k=1}^{N_v-1} \frac{N_v - k}{N_v}\Big[E_{v-v}(\rho k) + \Delta E_{int}(\rho k)\Big]. \quad \text{(S.12)}$$

The energy minimum $\min_\rho E_{tot/1v}$ determines the equilibrium period ρ_0 of the bound state, and is shown in Supplementary Figure 5c for different N_v. One can clearly observe that the vortex attraction becomes stronger for larger clusters. For a moderate regime ($\ell \lesssim \lambda$) the system prefers the formation of groups with small VP number N_v. Namely, at $\ell/\lambda = 0.25$, the most favourable are three-VP clusters with a small internal size $\rho_0 \ll \lambda$. This generally means that a long vortex chain is unstable with respect to the decay into small clusters separated by a large ($\gtrsim \lambda$) distance from each other (see Supplementary Figure 5a). Since the real material contains impurities and other types of mesoscopic inhomogeneities, the pinning of the VP and, consequently, the coexistence of clusters of different sizes are expected. Noteworthy, the same kind of effect has been predicted for completely different system of tilted vortices in thin anisotropic superconductors [9–11].

We believe this to be a reasonable interpretation of the results observed in the experiment (see Fig. 4). One can understand the appearance of the magnetic bubbles as a "fine-tuning effect": there is a specific range of $\ell \lesssim \lambda$ (controlled by the temperature) at which the stable multi-VP structures exist. At $\ell \gg \lambda$ the polaron effect is almost absent, while at $\ell \ll \lambda$ it may lead to the vortex generation instability, which requires additional investigation both from theory and experiment.

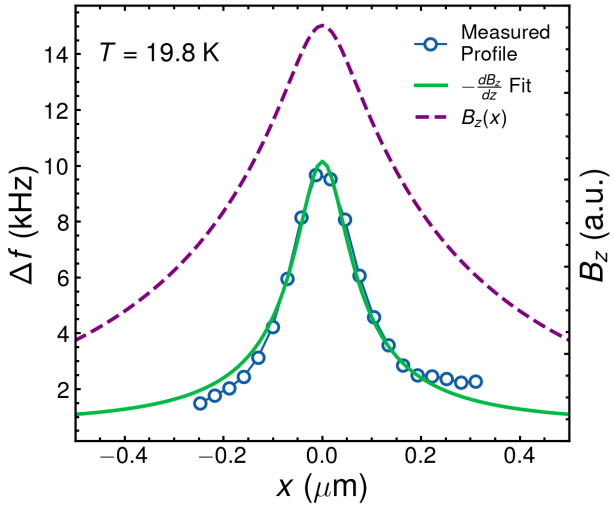

Supplementary Figure 6. **Example MFM vortex profile and fit result.** A profile of a single vortex taken from an MFM measurement at $T = 19.8$ K (blue circles). The data are fitted to equation S.15 (green line) yielding a scan height of $z = 49$ nm. The corresponding B_z of the vortex is plotted in comparison (purple dashed line).

SUPPLEMENTARY NOTE 6: MODELLING VORTEX PROFILES

The magnetic force microscopy (MFM) vortex profiles were modelled using the Clem variational model[12] modified to account for surface screening effects following an approach due to Kirtley *et al.* [13] assuming a variational coherence length $\xi_v(0) = 4.604$ nm. A Gorter-Casimir two fluid model temperature dependence has been assumed for the penetration depth, $\lambda(T) = \lambda(0)/\sqrt{1-(T/T_c)^4}$, with $\lambda(0) = 350$ nm[14]. The model provides the following description of the z-component of the B field due to a vortex:

$$B_z(x,y,z) = \frac{\phi_0}{2\pi\lambda}\int_0^\infty \frac{K_1(\sqrt{q^2+\lambda^{-2}\xi_v})}{(\sqrt{q^2+\lambda^{-2}}+q)K_1(\xi_v/\lambda)} J_0(q\sqrt{x^2+y^2})\exp(-qz)q\,dq\,, \tag{S.13}$$

where z is the scan height of the MFM sensor above the surface of the superconductor and has been treated here as a fit parameter. As discussed in the Methods section of the manuscript, the measured MFM frequency shifts ($\Delta_f = \Delta f_x + \Delta f_y$) are proportional to $\partial B_x/\partial x + \partial B_y/\partial y = -\partial B_z/\partial z$, and described in our model by

$$-\frac{dB_z}{dz}(x,y,z) = \frac{\phi_0}{2\pi\lambda}\int_0^\infty \frac{K_1(\sqrt{q^2+\lambda^{-2}\xi_v})}{(\sqrt{q^2+\lambda^{-2}}+q)K_1(\xi_v/\lambda)} J_0(q\sqrt{x^2+y^2})\exp(-qz)q^2\,dq\,. \tag{S.14}$$

In practice, due to the way the MFM data were recorded, the fits shown in the manuscript were made utilising three free parameters: the scan height z, a proportionality constant α and an arbitrary offset β, i.e. :

$$\Delta f_x + \Delta f_y = \alpha\frac{dB_z}{dz}(x,y,z) + \beta\,. \tag{S.15}$$

An example of the result of fitting a single vortex to S.15 at 19.8 K is shown in Supplementary Figure 6 with fit parameters $z = 49$ nm, $\alpha = 0.072$ kHz/G and $\beta = 0.862$ kHz (assuming values of $\lambda(19.8\,\mathrm{K}) = 462$ nm and $\xi_v(19.8\,\mathrm{K}) = 10.5$ nm). Also plotted is an arbitrarily scaled version of $B_z(x,0,z)$ for the same scan height. Note how the MFM technique renders a much narrower version of the vortex than if one measured the vortex magnetic fields directly, in this case by almost a factor of three.

The profiles of double vortices that are bound together by vortex polarons (i.e. those shown in Fig. 4), have been fitted to

$$\Delta f_x + \Delta f_y = \alpha\left(\frac{dB_z}{dz}(x,y+\frac{w}{2},z) + \frac{dB_z}{dz}(x,y-\frac{w}{2},z)\right) + \beta\,, \tag{S.16}$$

where the additional fit parameter w is the lateral separation between the two vortex cores.

SUPPLEMENTARY REFERENCES

[1] Bean, C. P. Magnetization of High-Field Superconductors. *Rev. Mod. Phys.* **36**, 31-39 (1964).

[2] Gyorgy, E. M., van Dover, R. B., Jakcson, K. A., Schneemeyer, L. F. & Waszczak, J. V. Anisotropic critical currents in $Ba_2YCu_3O_7$ analyzed using an extended Bean model. *Appl. Phys. Lett.* **55**, 283 (1989)

[3] Eley, S., Miura, M., Maiorov, B. & Civale, L. Universal lower limit on vortex creep in superconductors. *Nat. Mater.* **16**, 409-413 (2017).

[4] Iwasa, Y. *Case Studies in Superconducting Magnets: Design and Operational Issues, Second Edition* (Springer US, Boston, MA, 2009).

[5] Della Torre, E. *Magnetic Hysteresis* (IEEE Press, New York, 1999)

[6] Yeshurun, Y., Malozemoff, A. P. & Shaulov, A. Magnetic relaxation in high-temperature superconductors. *Rev. Mod. Phys.* **68**, 911-949 (1996).

[7] Fauré, M. & Buzdin, A. Domain Structure in a Superconducting Ferromagnet. *Phys. Rev. Lett.* **94**, 187202 (2005)

[8] Tinkham, M. *Introduction to Superconductivity, Second Edition* (Dover Publications Inc, Mineola, NY, 2004).

[9] Samokhalov, A. V, Savinov, D. A., Mel'nikov, A. S. & Buzdin, A. I. Vortex clusters and multiquanta flux lattices in thin films of anisotropic superconductors. *Phys. Rev. B* **82**, 104511 (2010)

[10] Samokhalov, A. V., Mel'nikov, A. S. & Buzdin, A. I. Attraction between pancake vortices and vortex molecule formation in the crossing lattices in thin films of layered superconductors. *Phys. Rev. B* **85**, 184509 (2012)

[11] Buzdin, A. I., Mel'nikov, A. S. & Samokhalov, A. V. Vortex Molecules in Thin Films of Layered Superconductors. *J. Supercond. Nov. Magn.* **26**, 2853-2857 (2013)

[12] Clem, J. R. Simple Model for the Vortex Core in a Type II Superconductor. *J. Low Temp. Phys.* **18**, 427-434 (1975).

[13] Kirtley, J. R. *et al.* Upper limit on spontaneous supercurrents in Sr_2RuO_4. *Phys. Rev. B* **76**, 014526 (2007)

[14] Stolyarov, V. S. *et al.* Domain Meissner state and spontaneous vortex-antivortex generation in the ferromagnetic superconductor $EuFe_2(As_{0.79}P_{0.21})_2$. *Sci. Adv.* **4**, eaat1061; 10.1126/sciadv.aat1061 (2018).